The Astrophysical Journal, 934:38 (15pp), 2022 July 20 https://doi.org/10.3847/1538-4357/ac7785
© 2022. The Author(s). Published by the American Astronomical Society.
OPEN ACCESS

Quantifying Properties of Photospheric Magnetic Cancellations in the Quiet Sun Internetwork

Vincent E. Ledvina[1,2], Maria D. Kazachenko[2,3], Serena Criscuoli[2], Dennis Tilipman[2,3], Ilaria Ermolli[4], Mariachiara Falco[5], Salvatore Guglielmino[5], Shahin Jafarzadeh[6,7], Luc Rouppe van der Voort[7,8], and Francesca Zuccarello[9]

[1] University of North Dakota, 101 Cornell St., Grand Forks, ND 58202; USA; vincentledvina@gmail.com
[2] National Solar Observatory, 3665 Discovery Drive, Boulder, CO 80303, USA
[3] Dept. of Astrophysical and Planetary Sciences, University of Colorado Boulder, 2000 Colorado Ave, Boulder, CO 80305, USA
[4] INAF—Osservatorio Astronomico di Roma, Via Frascati 33, Monte Porzio Catone, RM, I-00078, Italy
[5] INAF—Catania Astrophysical Observatory, Via Santa Sofia 78, I-95123 Catania, Italy
[6] Max Planck Institute for Solar System Research, Justus-von-Liebig-Weg 3, D-37077 Göttingen, Germany
[7] Rosseland Centre for Solar Physics, University of Oslo, P.O. Box 1029 Blindern, NO-0315 Oslo, Norway
[8] Institute of Theoretical Astrophysics, University of Oslo, P.O. Box 1029 Blindern, NO-0315 Oslo, Norway
[9] Dipartimento di Fisica e Astronomia "Ettore Majorana"—Sezione Astrofisica, Università di Catania, Via Santa Sofia 78, I-95123 Catania, Italy
Received 2021 October 22; revised 2022 June 7; accepted 2022 June 8; published 2022 July 22

Abstract

We analyzed spectropolarimetric data from the Swedish 1 m Solar Telescope to investigate the physical properties of small-scale magnetic cancellations in the quiet Sun photosphere. Specifically, we looked at the full Stokes polarization profiles along the Fe I 557.6 nm and of the Fe I 630.1 nm lines measured by the CRisp Imaging SpectroPolarimeter to study the temporal evolution of the line-of-sight magnetic field during 42.5 minutes of quiet Sun evolution. From this magnetogram sequence, we visually identified 38 cancellation events. We then used the *Yet Another Feature Tracking Algorithm* to characterize the physical properties of these magnetic cancellations. We found on average 1.6×10^{16} Mx of magnetic flux canceled in each event with an average cancellation rate of 3.8×10^{14} Mx s^{-1}. The derived canceled flux is associated with strong downflows, with an average speed of $V_{\rm LOS} \approx 1.1$ km s^{-1}. Our results show that the average lifetime of each event is 9.2 minutes with an average of 44.8% of initial magnetic flux being canceled. Our estimates of magnetic fluxes provide a lower limit since studied magnetic cancellation events have magnetic field values that are very close to the instrument noise level. We observed no horizontal magnetic fields at the cancellation sites and therefore cannot conclude whether the events are associated with structures that could cause magnetic reconnection.

Unified Astronomy Thesaurus concepts: Solar magnetic fields (1503); Solar surface (1527); Solar photosphere (1518); The Sun (1693); Solar magnetic flux emergence (2000); Solar physics (1476)

1. Introduction

The Sun has historically been divided into two domains: the active Sun and the quiet Sun (QS). The active Sun is commonly defined as areas of the Sun occupied by active regions, plage, and sunspots while the QS represents the remaining areas. It is reported that in the early stages of solar physics, scientists believed the QS to be nonmagnetic because only granular convection could be seen in continuum images (e.g., Bellot Rubio & Orozco Suárez 2019). However, early measurements showed that magnetic features are ubiquitous on the Sun. For example, using the Kitt Peak magnetograph, Livingston & Harvey (1971) reported a background internetwork (IN) field level of 2–3 G. Recent spectropolarimetric measurements allow magnetic structures to be observed down to scales at the limits imposed by current spatial resolution (e.g., Danilovic et al. 2010). These can be analyzed by using new inversion techniques to interpret the Zeeman and Hanle effects (e.g., del Toro Iniesta & Ruiz Cobo 2016). Quite the opposite of nonmagnetic, the QS displayed a reticular pattern of intense kilogauss fields, the magnetic network (NE), and a varied distribution of smaller-scale (sub-arcsec) magnetic flux concentrations in the areas between them—the solar IN (e.g., Gošić et al. 2014). State-of-the-art, three-dimensional magnetohydrodynamic simulations of the solar atmosphere (e.g., Rempel 2014) indicate that a large part of the solar surface magnetic features is still unresolved.

Studies by Gošić et al. (2016) and others (e.g., Sánchez Almeida 2004) have indicated that IN fields are essential contributors to the Sun's overall magnetic flux output, with the transport of magnetic flux to the solar photosphere at a rate of 120 Mx cm^{-2} day^{-1}, which is significantly higher than the 1 Mx cm^{-2} day^{-1} transported by active regions (Thornton & Parnell 2011). A large portion of that flux is transported to neighboring intergranular lanes via convective motions (Martínez González & Bellot Rubio 2009) and then to the NE supergranular boundaries (Livingston & Harvey 1975; Zirin 1985; Bellot Rubio & Orozco Suárez 2012). These motions make the IN capable of generating a complete magnetic flux resupply of the surrounding NE within only ≈10 hr (Gošić et al. 2014) indicating that they are an important contributor to the greater flux output of the solar photosphere. QS magnetism has in fact been suggested to affect global solar properties such as limb darkening (e.g., Criscuoli & Foukal 2017), photospheric temperature gradient (e.g., Faurobert et al. 2016), and global radiative output (e.g., Rempel 2020, and references therein).

Original content from this work may be used under the terms of the Creative Commons Attribution 4.0 licence. Any further distribution of this work must maintain attribution to the author(s) and the title of the work, journal citation and DOI.

The transient nature of the IN manifests in frequent instances of magnetic flux emergence, dissipation, and cancellation events. IN magnetic flux cancellation is one of three processes (flux decay, cancellation, and interaction with NE) in which flux is removed from the photosphere, and is a mechanism that leads to the maintenance of the flux budget in the photosphere (Schrijver et al. 1997; Lamb et al. 2013; Gošić et al. 2016). A physical cancellation event results in an in situ disappearance of magnetic flux from the solar photosphere as a result of the interactions between two opposite-polarity magnetic elements (Livi et al. 1985; Martin et al. 1985). Cancellations are a contributor to QS magnetic behavior and have been observed to play a critical role in many dynamic upper-atmosphere solar phenomena, such as coronal mass ejections, flares, and filament eruptions (Wang et al. 1996; Zhang et al. 2001; Zuccarello et al. 2007; Chintzoglou et al. 2019; Yardley et al. 2016) as well as the formation of prominences (Denker & Tritschler 2009), coronal jets (Panesar et al. 2016), and Ellerman bombs (Schmieder et al. 2002).

IN cancellations may also partially drive the heating of the chromosphere. Gošić et al. (2018) identified 51 cancellation events using data from the Swedish 1 m Solar Telescope (SST; Scharmer et al. 2003a) and compared these with chromospheric temperature diagnostics using IRIS data (De Pontieu et al. 2014). Magnetic cancellations were found to release enough energy to provide local brightening in the chromosphere (Gosic et al. 2017, 2021).

The derivation of statistical properties of IN cancellations is among the most important steps in further understanding their role in other solar phenomena. This is somewhat challenging due to the relatively low signal-to-noise ratio in current polarimetric measurements of the QS. IN fields are particularly difficult to observe because they are arranged on small spatial scales, evolve rapidly, and individually, produce very weak signals. Thus, major advances in this research area have mainly been brought about by advances in observing technologies (instruments with higher spectropolarimetric sensitivity and spatial and temporal resolutions) and new computational modeling, meaning that many of the fundamental aspects of IN cancellations have been discovered recently and are still widely disputed and incomplete.

In this paper, we analyzed a small area of the QS observed at the SST with high spatial resolution and high cadence spectropolarimetric data. In these data, we noted numerous signatures of magnetic cancellation events, and we describe in the following their statistical properties. Our results complement a growing list of publications focusing on QS magnetism and the important process of cancellations that pervade its surface (e.g., Chae et al. 2002, 2004; Kaithakkal & Solanki 2019; Guglielmino et al. 2012; Nisenson et al. 2003).

The outline of this paper is as follows: In Section 2, we describe SST observations and our analysis in Section 3. In Section 4.1, we describe a single cancellation event in detail. In Section 4.2, we summarize the statistical parameters of the physical quantities estimated for all 38 cancellation events. In Section 5, we discuss our findings and their implications in the broader field of QS research. In the Appendix, we describe four additional cancellation events in detail.

2. Observations

We employed the full Stokes polarization profiles along the Fe I 557.6 and 630.1 nm lines to analyze the temporal evolution of the magnetic field and the dynamic properties of plasma at cancellation sites.

Specifically, for our analysis we used data acquired at the SST (Scharmer et al. 2003a) in La Palma, Spain, with the CRisp Imaging SpectroPolarimeter (CRISP; Scharmer et al. 2008), as part of a 2 week long campaign (2011 August 6–18). These observations captured a QS region at the disk center on 2011 August 6, beginning at 07:57:39 UTC and lasting for 42.5 minutes.

CRISP acquired data along the Fe I 630.1, 630.2, and 557.6 nm lines spectral ranges. Only data acquired along the 630.1 and 557.6 nm lines were used in this study. The pixel scale was $\approx 0\farcs059$ pixel^{-1} with a field of view of $57\farcs5 \times 57\farcs3$. A total of 100 scans were acquired with a temporal cadence of 28 s. Raw data were calibrated using an early version of the standard CRISP calibration pipeline (CRISPRED; de la Cruz Rodríguez et al. 2015). The SST adaptive optics system (Scharmer et al. 2003b) was able to make continuous corrections to the wavefront, effectively operating at a 100% lock rate. The combination of the use of adaptive optics and of the application of the Multi-Object Multi-Frame Blind Deconvolution image restoration technique (van Noort et al. 2005) allowed for effective minimization of seeing-induced aberrations. The images studied here had an angular resolution of $\approx 0\farcs15$ at 557.6 nm, which is close to the diffraction limit of the SST. The estimated spectropolarimetric sensitivity was $\approx 3 \times 10^{-3}$.

This data set has been employed in previous studies to investigate the dynamics (Stangalini et al. 2015, 2017) and thermal properties (Cristaldi & Ermolli 2017; Viavattene et al. 2021) of plasma in the QS regions. These studies were made possible in part due to the high resolution of the SST and its instruments, inspiring us to analyze the same data to investigate small magnetic features on the QS surface.

We derived information about the magnetic properties of the plasma using the four Stokes parameters, I, Q, U, and V observed in the Fe I 630.1 nm line. Specifically, we derived the line-of-sight (LOS) magnetic field $B_{\rm LOS}$ from the separation of the centroids of the $I+V$ and I–V signals, estimated with the center-of-gravity (COG) method (Rees & Semel 1979; Uitenbroek 2003):

$$B_{\rm LOS} = \frac{\lambda_+ - \lambda_-}{2}\frac{4\pi mc}{eg_L\lambda_0^2}, \tag{1}$$

where g_L is the line's effective Landé factor, m and e are the electron mass and charge, respectively, λ_0 is the central wavelength of the line, and $\lambda_\pm$ are defined as

$$\lambda_\pm = \frac{\int \lambda(I_c - (I \pm V))d\lambda}{\int (I_c - (I \pm V))d\lambda}, \tag{2}$$

where I_c is the line's nearby continuum intensity. The total circular polarization signal (TCP; del Toro Iniesta 2007) was computed as

$$\mathrm{TCP} = \int_\lambda \frac{V(\lambda)}{I_c}d\lambda, \tag{3}$$

and the total linear polarization (TLP) signal (del Toro Iniesta 2007) as

$$\mathrm{TLP} = \int_\lambda \frac{\sqrt{Q(\lambda)^2 + U(\lambda)^2)}}{I_c}d\lambda. \tag{4}$$

To estimate the LOS velocities ($V_{\rm LOS}$), we used the Doppler shift of the core of the magnetically insensitive Fe I 557.6 nm line. The line core was estimated by fitting the observed line

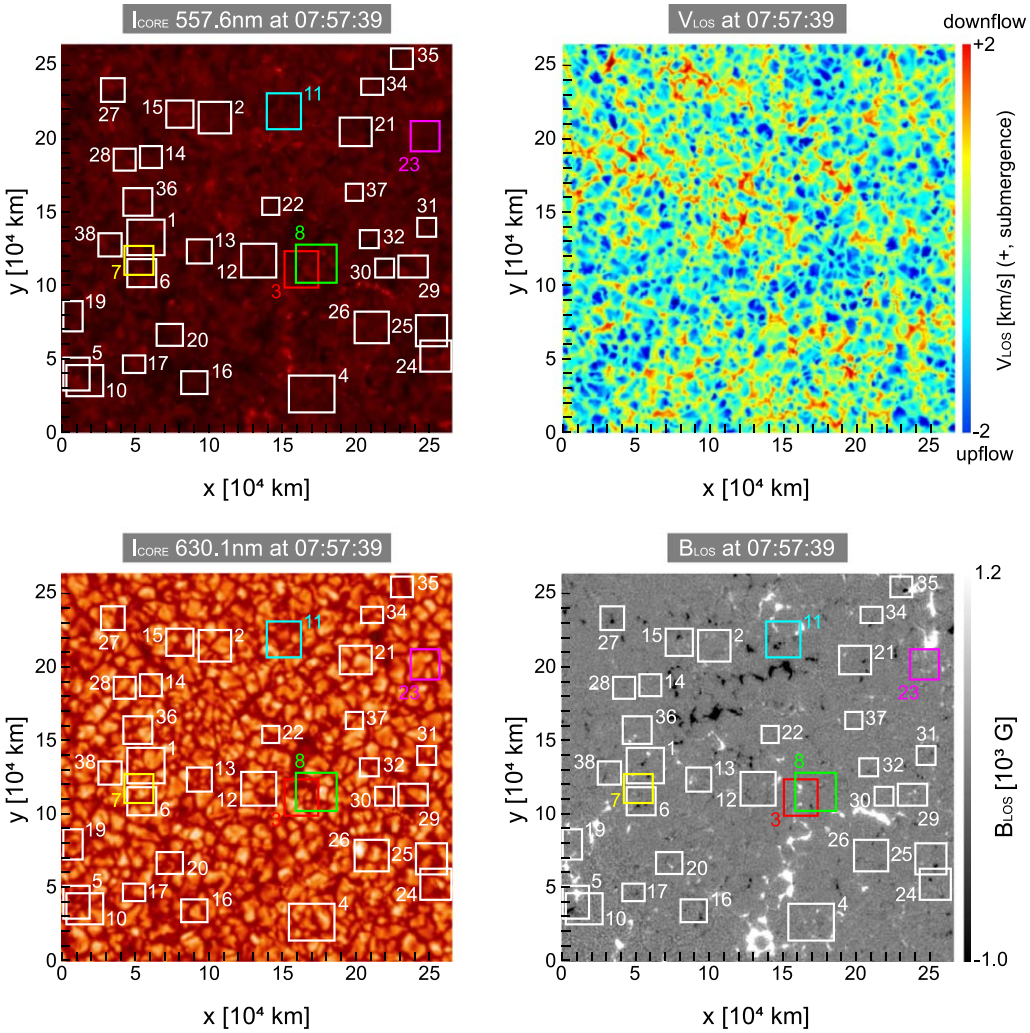

Figure 1. Four snapshot views of a QS region at the disk center, as observed by the SST. *Top left*: core intensity in the nonmagnetic Fe I 557.6 nm line. *Top right*: LOS velocity ($V_{\rm LOS}$) with positive and negative values corresponding to downflows and upflows, respectively. *Bottom left*: continuum image at Fe I 630.1 nm. *Bottom right*: LOS magnetogram ($B_{\rm LOS}$). Rectangles indicate the analyzed regions of interest, numbered by the ROI indices. Colored rectangles represent the events described in Section 4.1 and the Appendix of this manuscript.

profiles with a Gaussian function, and the Doppler shift was computed taking as reference the core position of the average line profile computed over the whole time series. The resulting average velocity over the whole field of view is -0.07 ± 0.035 km s^{-1}. Indeed, this value is around the *convective upflow* value for the line found in Dravins et al. (1981). This is approximately -0.15 to -0.2 km s^{-1} at the disk center.

Examples of the data and data products used in our analysis are shown in Figure 1: the continuum intensities in the Fe I 557.6 and 630.1 nm continua (left column) and the derived $V_{\rm LOS}$ and $B_{\rm LOS}$ (right column).

3. Data Analysis

We used the TCP sequence to visually identify 38 cancellation events for our analysis. We defined the following criteria for our selection. First, for visual detection simplicity, we chose cancellations that involve two opposite-sign polarities of roughly equal size. While the choice of same-size polarities simplifies the process of the cancellation search, it leads to an underestimation of canceled magnetic flux. Second, we avoided selecting events where same-signed flux recombined or emerged in the same location. Finally, we only selected cancellations where the polarities involved were visually identifiable. The average size of a region of interest (ROI) was $\approx 2 \times 10^5$ km^2. Given these criteria, we identified 38 cancellation ROI, shown as squares in Figure 1.

For each cancellation identified, we then applied the following three-step process: (1) feature tracking, (2) relabeling, and (3) polarity inversion line (PIL) identification. Examples of the three steps are illustrated in Figure 2 for five events. For context, the PIL is the boundary between opposite-polarity features. In the first step (second column in Figure 2), to identify individual magnetic features we used *Yet Another Feature Tracking Algorithm* (YAFTA) solar magnetic tracking algorithm (Welsch et al. 2004). YAFTA has been shown to reliably identify small and short-lived magnetic features. It identifies magnetic features using a gradient-based *downhill* method that dilates local flux maxima by expanding down the gradient toward zero flux density. To discriminate the false positives, YAFTA allows the user to control the following parameters: a threshold for a minimum magnetic field to consider ($B_{\rm min}$), a saddle threshold for a minimum magnetic field to merge the already selected features ($B_{\rm saddle}$), and a minimum area size for feature identification ($S_{\rm min}$). In our

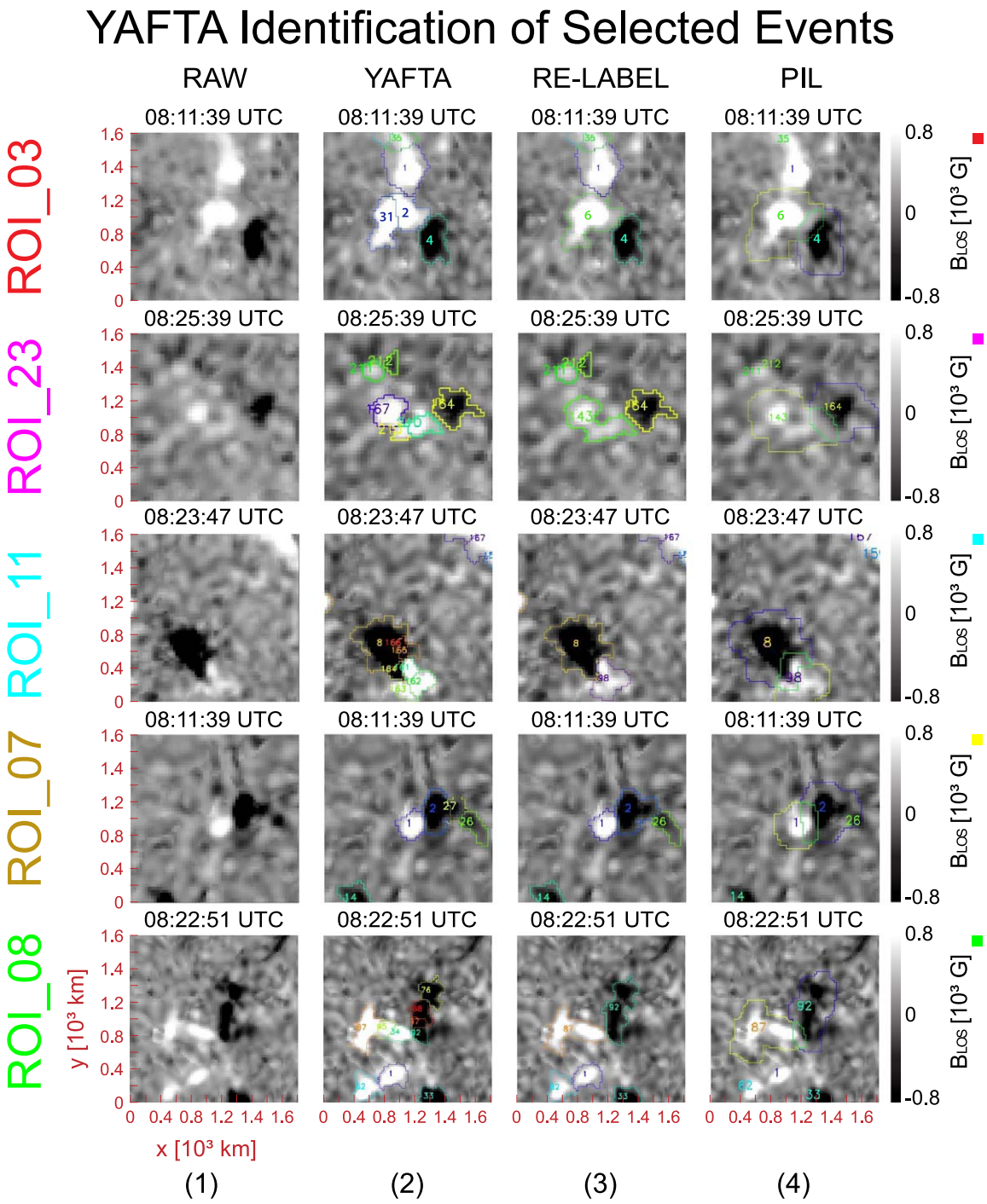

Figure 2. $B_{\rm LOS}$ time snapshots of five distinct cancellations showing the different steps of processing with YAFTA, as described in Section 2. Column (1) shows a raw magnetogram image of the ROI. Column (2) shows the initial tracking result with YAFTA. Column (3) shows the relabeled features. Column (4) shows the two canceling features, their dilated masks, and PIL (green outline). Each row of images represents a different ROI. The color of the square beside the rightmost image corresponds to the color of the ROI in the full field-of-view magnetogram shown in Figure 1.

analysis, we chose $B_{\rm min} = 40$ G, $B_{\rm saddle} = 80$ G, and $S_{\rm min} =$ 4 pixels. This parameter set resulted in tracking runs that consistently identified features above the noise level without false positives. Use of lower thresholds for $B_{\rm min}$ resulted in incorrect feature identification in the noisy areas and larger values of feature magnetic fluxes. The thresholds were set based on many tests and visual inspection of results. DeForest et al. (2007) report the effects of various thresholds used with YAFTA and their implications on feature tracking. After features are identified, YAFTA arbitrarily labels them based on its first pass through the data. In the second step (third column in Figure 2), since occasionally YAFTA incorrectly assigned multiple labels to one feature, we had to manually relabel all the features after the initial tracking. This incorrect assignment is due to the fact that YAFTA struggles with very large or strong and very small or weak magnetic elements, reflecting imperfections in our approach. After the second pass, the feature masks could be referenced and magnetic properties could be analyzed for each polarity independently. Finally, to describe the Doppler velocities associated with each

cancellation event, we examined the Doppler velocity properties within the PIL. To define PIL location (fourth column in Figure 2), we dilated the masks of the two canceling polarities by 2 pixels and defined the PIL as the region where these two masks overlapped.

To describe each cancellation event we used the following set of parameters: magnetic flux, Φ_B, flux cancellation rate, R, specific cancellation rate, r, convergence speed, $V_{\rm conv}$, and Doppler velocity, $V_{\rm LOS}$. We used these parameters as the foundation of our analysis.

For each observation at time t in the image sequence we defined the unsigned magnetic flux of positive (+) and negative (−) polarities in each pair, i, as

$$\Phi_{B,i}(t) = \sum_{j=1}^{N_i} |B_j(t)|\ ds^2 = |\Phi_{B,i-}| + |\Phi_{B,i+}|, \tag{5}$$

where N_i is the number of magnetic field values in the polarity pair, B_j is the magnetic field value at each pixel, j, and ds is the pixel size ($0\farcs059$ pixel^{-1}).

The position at time t of each positive and negative polarity in the pair is defined as the center of gravity $\mathrm{COG_i}(t) = [x_i(t), y_i(t)]$, i.e., the mean position of the feature weighted by the magnetic flux:

$$x_i(t) = \frac{\sum_{j=1}^{N_i} x_j |B_j|\ ds^2}{\Phi_{B,i}},$$
$$y_i(t) = \frac{\sum_{j=1}^{N_i} y_j |B_j|\ ds^2}{\Phi_{B,i}}. \tag{6}$$

We then used these to calculate the separation distance, $g(t)$, and the convergence velocity, $v_{\rm conv}(t)$, between positive and negative polarities in each pair (Chae et al. 2002):

$$g_i(t) = |\mathrm{COG}_{i+}(t) - \mathrm{COG}_{i-}(t)|,$$
$$v_{\mathrm{conv,i}}(t) = -0.5\frac{dg_i(t)}{dt}. \tag{7}$$

To describe the amount of flux canceled we defined the flux cancellation rate, R_i, and the specific cancellation rate (rate per unit PIL length), r_i:

$$R_i(t) = \frac{d\Phi_{B,i}}{dt},\ \ r_i(t) \equiv R_i(t)/l_i(t), \tag{8}$$

where l_i is the length of the PIL separating the positive and negative polarities of each pair i.

Finally, we found the canceled flux as the difference between the flux values at the start time ($t_{\rm start}$) and end time ($t_{\rm end}$) of a cancellation event, so that the positive values indicated canceled flux:

$$\Delta\Phi_{B,i} = \Phi_{B,i}(t_{\rm start}) - \Phi_{B,i}(t_{\rm end}). \tag{9}$$

To describe the variability of $Ri(t)$ over time we also calculated the average and peak cancellation rates, $R_{\rm avg}$ and $R_{\rm peak}$, respectively, over duration, T, of each cancellation event. In the case of complete disappearance of the feature, we defined the last frame before disappearance as $t_{\rm end}$, when the magnetic flux was above zero.

To define the duration, T, of each cancellation event, we used the time when the PIL was defined, which occurred when opposite polarities were in close proximity to one another. In the events we observed, while the general trend of the polarities' fluxes was characterized by a decay, sometimes flux momentarily increased during the event, so the PIL was defined in the aforementioned way in order to capture the entire event as a whole. If during a cancellation event, one of the polarities dipped below the detection threshold for fewer than 5 frames but was seen thereafter, we considered it as one cancellation event.

To calculate $V_{\rm LOS}$, we averaged the Doppler velocity across the PIL region. Positive values were plasma submergence or downflows, while negative values were emergences or upflows. To describe the $V_{\rm LOS}$ variability, we used the mean and the peak values of $V_{\rm LOS}$, $V_{\rm LOS,avg}$, and $V_{\rm LOS,peak}$, respectively. To describe the change in Doppler velocity from the start to the end of the cancellation event we used

$$\Delta V_{{\rm LOS},i} = V_{{\rm LOS},i}(t_{\rm start}) - V_{{\rm LOS},i}(t_{\rm end}). \tag{10}$$

This formalism allowed us to account for cancellations taking place in intergranular lanes where plasma was already flowing downward or in areas where plasma was already flowing upward.

4. Results

Figure 1 shows a snapshot of the magnetogram sequence that we used to visually identify 38 distinct cancellation events. Note that we visually inspected the magnetogram to select cancellations in the IN regions away from the strong field regions belonging to the NE patches. In this section, we first present our results for one example cancellation event (Section 4.1) and then the statistical analysis for all 38 events (Section 4.2). The evolution of an additional four exemplary regions is provided in the Appendix.

4.1. Example of Individual Cancellation Event, ROI_03

Figure 3 (top row) shows the evolution of the magnetic field in one example event, ROI 3 (ROI_03). We chose to give this event special attention since it showed a marked flux cancellation, allowing us to compare the Doppler velocity in the PIL region before and during the cancellation. Furthermore, the polarities in this region were easy to identify by eye and there was very noticeable flux cancellation in both regions.

From the beginning of its detection, ROI_03 contained positive and negative polarities with relatively equal magnetic flux. Around 10 minutes into the tracking run, the two polarities became entangled (see the PIL region in Figure 3 panel (2a). Around 6 minutes after the PIL was defined, or at around 08:11:11 UTC, the polarities began canceling, losing flux at an average rate of 4.9×10^{14} Mx s^{-1}. $V_{\rm LOS}$ in the PIL region shows a small submergence of 0.1 km s^{-1} when the PIL was first defined (Figure 3, panel (2c) but then increased to over 1 km s^{-1} after the cancellation intensified (Figure 3, panel (4c)). The event lasted 10 minutes before the negative polarity decreased below the instrument noise level as can be seen in Figure 3, panel (7a). During the cancellation, the positive and negative polarities lost 1.87×10^{17} and 2.48×10^{17} Mx, respectively, i.e., around 54.7% of the unsigned initial magnetic flux of the bipole. The cancellation took place in an intergranular lane as can be seen in the continuum and Doppler velocity images. As illustrated in Figure 4, before cancellation, the Doppler velocity of the PIL was ≈0.1 km s^{-1}. As both polarities started canceling, with the peak cancellation rate of 4.4×10^{15} Mx s^{-1} occurring at 08:16:35

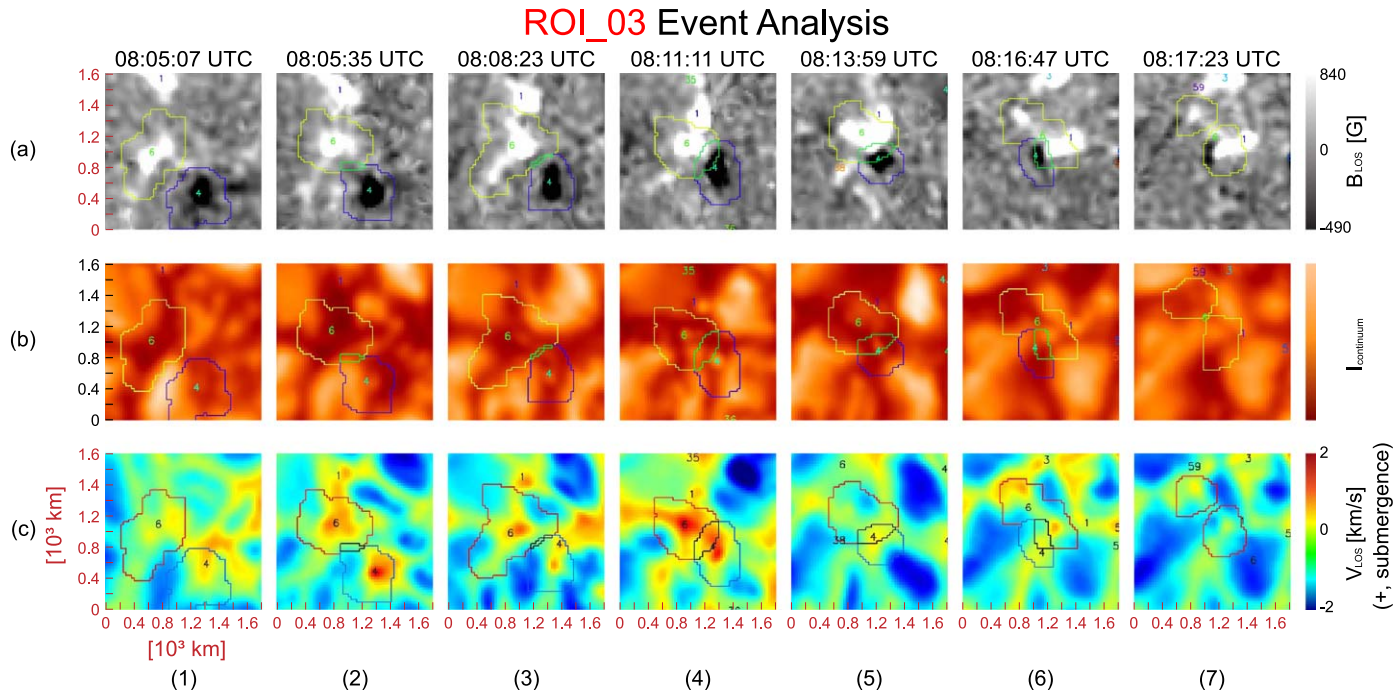

Figure 3. Evolution of $B_{\rm LOS}$ (top series), 630.1 nm intensity (middle series), and $V_{\rm LOS}$ (bottom series). ROI_03 in the time series begins with panel (1) (time immediately before PIL is defined) and progresses to panel (7) (time immediately after PIL is no longer defined).

UTC, the downflows at the PIL increased up to ≈ 1 km s^{-1}, persisting for approximately 5 minutes.

4.2. Results: Statistical Analysis of 38 Cancellation Events

We repeat the analysis described in the previous section for the 38 events in our data set. In Table 1, we present a summary of all events and major indices. In Table 2, we summarize our results showing cancellation parameters for the 38 cancellations events.

Duration: We found an average cancellation duration of $\approx$39.2 minutes. Cancellation lifetimes of 9 minutes were reported by de Wijn et al. (2008) and Gošić (2015) with a range of 1−22 minutes found by Gošić et al. (2018).

Initial magnetic flux: The distribution of initial fluxes, $\phi_{B,i}$, of the features can be seen in Table 2. and we see a distribution clustered around $[1-3] \times 10^{17}$ Mx. The observed magnetic flux is $[0.7-8.2] \times 10^{17}$ Mx. This wide range of values shows that our data set reflects the diversity of IN magnetic field strengths. The average value of $\bar{\Phi}_{B,i} = 3.3 \pm 0.3 \times 10^{17}$ Mx, and is lower than the value of 5.5×10^{17} Mx reported by Kaithakkal & Solanki (2019) and 6×10^{17} Mx reported by Guglielmino et al. (2012) but is nearly identical to the 3×10^{17} Mx reported by Gosic et al. (2012).

Canceled magnetic flux: Values of the magnetic flux change, $\Delta\Phi_B$, show a clustering below 10^{17} Mx ranging from 0.2×10^{17}–3.1×10^{17} Mx. We find the average canceled magnetic flux to be $\Delta\Phi_B = [1.6 \pm 0.16] \times 10^{17}$ Mx. Compared with the initial flux, this change corresponds to $[44.9 \pm 2.3]\%$ of the initial flux being canceled.

Cancellation rates: We found cancellation rates ranging from 0.3×10^{14}–7.4×10^{14} Mx s^{-1} with a mean cancellation rate of $3.8 \pm 0.5 \times 10^{14}$ Mx s^{-1}. Kaithakkal & Solanki (2019) found similar results for small magnetic elements with fluxes around 10^{17} Mx and flux decay rates of 4×10^{14} Mx s^{-1}. Our values were slightly larger than the 2.6×10^{14} Mx s^{-1} found by Guglielmino et al. (2012) and the 3.6×10^{14} Mx s^{-1} reported

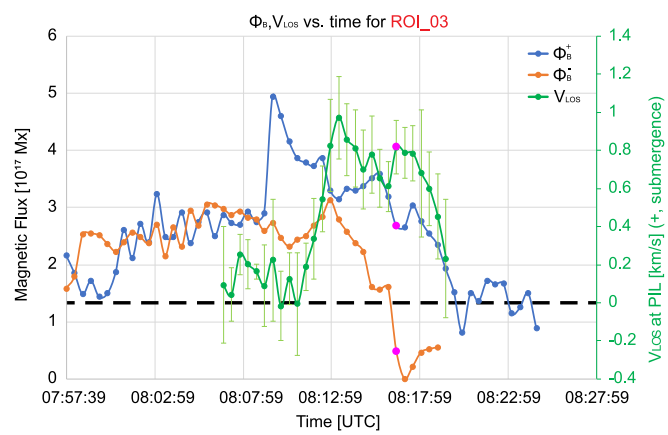

Figure 4. Evolution of LOS magnetic flux Φ_B and PIL mean Doppler velocity $V_{\rm LOS}$ in ROI_03. The blue data points represent Φ_B^+, and the orange points represent Φ_B^-. The pink dots represent the time when the maximum flux cancellation was achieved. The green data points represent $V_{\rm LOS}$, and are only counted while the PIL is defined. Positive values of $V_{\rm LOS}$ represent submergence. A dotted line is placed at $V_{\rm LOS} = 0$ km s^{-1} to aid in viewing the diagram.

by Chae et al. (2002). For all events we found the mean of the peak flux cancellation rate to be $R_{\rm peak} = 2.9 \pm 0.2 \times 10^{15}$ Mx s^{-1}, i.e., around one order of magnitude higher than the average rate, $R_{\rm avg}$.

Cancellation rates averaged over PIL length: We find the mean specific cancellation rate for all events to be $r = 2.7 \pm 0.5 \times 10^6$ G cm s^{-1}. Compared to Kaithakkal & Solanki (2019) (7.3×10^6 G cm s^{-1}) and Park et al. (2009) (8×10^6 G cm s^{-1}), our results are around 2 times smaller, but greater than the values obtained by Chae et al. (2002) (1.1×10^6 G cm s^{-1}) and nearly identical to the results of Litvinenko et al. (2007) (2.32×10^6 G cm s^{-1}).

Convergence speeds: For the 38 cancellation events we find the mean convergence speed $v_{\rm conv} = 0.6 \pm 0.07$ km s^{-1} with

Table 1
Summary Table Showing the Mean Values for 38 Magnetic Cancellations

Variable	This Work	Kaithakkal & Solanki (2019)	Chae et al. (2002)
$\Phi_{B,i}$ [10^{17} Mx]	3.3 ± 0.3	≈ 1.0	25
$\Delta\Phi_B$ [10^{17} Mx]	1.6 ± 0.2	…	…
$\Delta\Phi_B$ [%[a]]	44.9 ± 2.3	80	…
$R_{\rm avg}$ [10^{14} Mx s^{-1}]	3.8 ± 0.5	4.0	3.6
$R_{\rm peak}$ [10^{15} Mx s^{-1}]	2.9 ± 0.2	…	…
r [10^6 G cm s^{-1}]	2.7 ± 0.5	7.3	1.1
T [minutes]	39.2	3.3	…
$V_{\rm LOS,avg}$ [km s^{-1}]	0.5 ± 0.03	…	…
$V_{\rm LOS,peak}$ [km s^{-1}]	1.0 ± 0.04	1.4	…
$\Delta V_{\rm LOS}$ [km s^{-1}]	1.1 ± 0.03	…	…
$v_{\rm conv}$ [km s^{-1}]	0.6 ± 0.06	[0.3–1.8]	0.35

Note. $\Phi_{B,i}$ is the initial flux of the bipole, $\Delta\Phi_B$ is the amount of canceled flux, $R_{\rm avg}$ is the average rate of cancellation, $R_{\rm peak}$ is the peak rate of cancellation, r is the specific cancellation rate, T is the duration of the event, $V_{\rm LOS,avg}$ is the average Doppler velocity at the PIL, $V_{\rm LOS,peak}$ is the peak Doppler velocity at the PIL, $\Delta V_{\rm LOS}$ is the total change in Doppler velocity at the PIL, $v_{\rm conv}$ is the convergence velocity of the polarities, and a represents the percent of initial flux canceled; many cancellations ended below the noise floor.

values ranging from 0.2–2.1 km s^{-1}. Kaithakkal & Solanki (2019) reported a range of 0.3–1.8 km s^{-1}. These convergence speeds are similar to the supergranular flow velocities found by Litvinenko et al. (2007), Chae et al. (2002), and Iida et al. (2012). Still, we agree with Kaithakkal & Solanki (2019) that the wide distribution of convergence speeds as seen in individual cancellation events (see Figure 5) is evidence of the more chaotic flows found on granular scales. Using the average convergence speed to deduce whether cancellations are driven by supergranular motions or convective behavior is not entirely appropriate. According to Equation (7), polarities moving away would have a negative convergence speed. Averaging the unsigned speeds ($v_{\rm proper} = |v_{\rm conv}|$) produces a result that more accurately depicts the IN environment. Using an approach similar to that of Kaithakkal & Solanki (2019), we derived the proper motion speeds of the cancellations to be 0.9 ± 0.05 km s^{-1}, which is markedly higher than the convergence speeds. These proper motion speeds are more consistent with the rms velocity of magnetic elements in the IN areas found by Nisenson et al. (2003). Our results are also consistent with other studies of magnetic cancellations, e.g., Yang et al. (2009) reported proper motion speeds around 1 km s^{-1} while Kaithakkal & Solanki (2019) observed proper motion speeds higher than convergence speeds calculated using the traditional COG method (as can be seen in Figure 5). Keys et al. (2011) also noted that the horizontal velocity of merging bright points is $\approx$1 km s^{-1} and higher than the speed of isolated bright points.

Downflow speeds: Across the 38 cancellations we observed average downflows of $V_{\rm LOS,avg} = 0.5 \pm 0.03$ km s^{-1} and mean peak downflow speeds of $V_{\rm LOS,peak} = 0.6 \pm 0.1$ km s^{-1}. These high downflow speeds observed at flux cancellation sites are consistent with results from Chae et al. (2004). Harvey et al. (1999) found that emission structures from IN magnetic cancellations lasted longer in the photosphere than in the chromosphere and corona, concluding that magnetic flux is retracting below the surface. Analyzing the magnetic elements overlaid on the continuum images (i.e., Figure 3 panels (1–7b)), we noticed that many magnetic bipoles began cancellation in upflow regions and ended in downflow lanes, most likely due to convective motions. This was also observed by Kaithakkal & Solanki (2019). To explore this phenomenon we compared the $\Delta V_{\rm LOS}$ to the $V_{\rm LOS,avg}$, shown in Figure 6. This would indicate whether small outlier values of $V_{\rm LOS,avg}$ simply resulted from a greater downflow shift from local upflow convection. We see that although the mean $V_{\rm LOS,avg} = 0.5 \pm 0.03$, the $\Delta V_{\rm LOS} = 1.1 \pm 0.07$. There is no statistically significant relationship between $\Delta V_{\rm LOS}$ and $V_{\rm LOS,avg}$ (the Pearson correlation coefficient, $\rho = 0.07$).

Investigating further correlations between $V_{\rm LOS}$ and other statistical parameters, we first addressed the hypothesis that more magnetic flux cancellation may lead to a higher downflow signature. We plotted $V_{\rm LOS,peak}$ versus $\Delta\Phi_B$ in Figure 7 and no correlation was found. Relationships between $\Delta V_{\rm LOS}$ and $\Delta\Phi_B$, and $V_{\rm LOS,avg}$ versus $\Delta\Phi_B$ were also plotted but are not shown in the manuscript; the analysis found no correlation. R^2 values were 0.04, 0.004, and 0.03 for the data sets, respectively. The notion that downflows may be limited by canceled flux, as if by a threshold, is not supported by these data. This finding may also suggest that the magnitude of downflows is more dependent on the magnitude of decay than its amount.

To investigate this notion, we plotted all $V_{\rm LOS}$ parameters against the average and peak flux cancellation rates, $R_{\rm avg}$ and $R_{\rm peak}$, respectively. We find that while there is statistical evidence to support cancellation events drive submergence, whether or not the submergences are a result of the magnetic cancellation or the typical downflows found in intergranular lanes where many polarities eventually coalesce and cancel is indeterminable from this initial analysis. As opposed to studying the effects of $\Delta\Phi_B$ on $V_{\rm LOS}$, $R_{\rm avg}$ and $R_{\rm peak}$ provide the best insight into how the physical process of magnetic cancellation relates to submergences, since timescales vary with differing amounts of $\Delta\Phi_B$. We investigate this in Figure 8, where we plotted $V_{\rm LOS,peak}$ vs. $R_{\rm peak}$ and found no correlation. Compared to typical submergence speeds in intergranular lanes, which have been reported as 0.30–0.50 km s^{-1} by Oba et al. (2017), the downflows associated with the cancellation events are much faster.

For $V_{\rm LOS}$ versus r, the specific cancellation rate, we find no correlation (Figure 9).

Analyzing single event performance we found a stronger correlation between peak Doppler velocity and specific cancellation rate than the analysis of the entire cancellation set. In ROI_03 (see Figure 3), we directly plotted $R(t)$ versus $V_{\rm LOS}$, finding a weak correlation. We hypothesize that this might be caused by the definition of magnetic cancellation stating that only one feature in the canceling pair is required to lose magnetic flux; the other participant may gain magnetic flux concurrently; therefore, R, which we define as $R(t) = R(t)^+ + R(t)^-$, the net decay of the bipole, is not entirely appropriate for these cases. Second, the measurement variability is so great that its effect can directly confound results. Given these postulates, from the first time step where cancellation occurred we averaged every 84 s, essentially time binning the values of R and $V_{\rm LOS}$ by 3. We find a weak correlation between unbinned values ($R^2 = 0.1558$) yet a moderate correlation with the binned values ($R^2 = 0.3779$). This can be seen more clearly in Figure 10.

As stated earlier, during cancellation events we see magnetic fields frequently below the instrument noise level, so it is possible a correlation between $V_{\rm LOS}$ and R would be more

Table 2
Key Parameters of All 38 Magnetic Cancellations

ROI #	$\Phi_{B,i}$ [10^{17} Mx]	$\Delta\Phi_B$ [10^{17} Mx]	R_{avg} [10^{14} Mx s^{-1}]	R_{peak} [10^{15} Mx s^{-1}]	r [10^6 G cm s^{-1}]	T [min]	$V_{LOS,peak}$ [km s^{-1}]	ΔV_{LOS} [km s^{-1}]	v_{conv} [km s^{-1}]
1	5.6	3.0	5.4	2.7	1.8	9.8	0.8	0.8	0.4
2	1.9	0.7	0.9	2.7	0.3	8.4	1.2	1.1	0.1
3	5.8	2.6	4.5	4.4	4.0	10.3	0.9	0.9	0.4
4	3.1	3.4	1.8	3.7	0.8	23.8	1.3	1.3	0.2
5	6.9	1.7	13.0	4.2	8.7	9.3	0.9	1.6	0.4
6	5.9	2.0	8.1	2.9	3.0	5.1	0.8	0.3	0.9
7	5.2	2.5	3.7	2.9	1.0	13.5	0.9	1.1	0.2
8	6.1	3.0	2.5	5.1	0.9	19.1	0.9	1.1	0.4
9	2.5	1.2	0.6	2.9	0.2	33.6	1.4	2.0	0.1
10	6.9	2.9	4.6	5.7	2.2	9.3	0.8	1.5	0.4
11	8.2	2.5	3.5	3.2	1.1	10.3	0.8	0.8	0.3
12	5.5	2.6	5.9	4.2	11.2	9.3	0.9	0.7	0.5
13	1.3	0.5	1.3	3.3	0.7	6.7	1.1	0.9	0.6
14	2.1	1.4	1.9	2.2	1.0	10.3	1.0	1.4	0.3
15	3.3	1.8	3.9	3.8	2.1	11.2	1.2	1.5	0.6
16	1.9	1.0	6.0	1.6	2.4	3.7	1.3	0.7	1.3
17	2.0	0.6	4.3	1.9	2.2	3.7	1.2	1.9	1.0
18	2.6	1.6	3.0	3.6	1.3	10.3	1.0	0.9	0.4
19	5.2	3.0	7.2	5.7	2.9	6.1	0.8	0.7	0.7
20	2.3	1.1	5.1	3.6	5.7	6.5	1.1	1.7	0.9
21	1.0	0.3	6.0	8.5	11.2	3.7	0.6	0.8	0.7
22	1.0	0.2	0.9	1.3	0.4	6.5	1.5	1.4	0.5
23	1.4	0.6	0.9	2.6	0.6	11.7	1.0	1.4	0.3
24	2.9	1.3	2.6	1.9	2.6	4.7	1.1	0.7	1.2
25	5.7	2.9	3.9	3.5	2.7	15.4	0.9	1.2	0.1
26	4.0	1.7	3.2	2.8	6.1	10.7	0.9	1.2	0.6
27	9.4	0.5	2.2	1.2	3.7	5.1	1.3	1.3	0.8
28	3.2	0.6	1.8	2.4	0.6	10.7	0.9	1.0	0.4
29	4.1	1.4	3.3	2.2	1.3	7.0	0.8	0.6	0.7
30	1.2	0.7	1.0	1.1	0.6	7.0	1.4	1.3	0.6
31	7.5	0.3	2.7	1.3	1.2	3.2	0.7	0.3	1.1
32	1.2	0.5	1.3	1.1	1.3	7.0	0.9	0.8	0.7
33	2.8	1.3	2.9	2.4	1.4	5.6	0.2	1.0	0.7
34	2.3	0.7	9.4	3.5	0.6	11.2	0.7	1.1	1.0
35	3.5	2.3	4.2	5.1	2.1	10.3	0.6	0.9	0.3
36	3.4	2.3	1.4	3.8	9.5	2.8	0.9	0.3	2.1
37	1.9	0.1	2.0	1.9	0.4	3.2	1.0	0.5	0.8
38	4.9	0.7	3.8	3.8	3.5	3.2	1.3	1.5	0.2

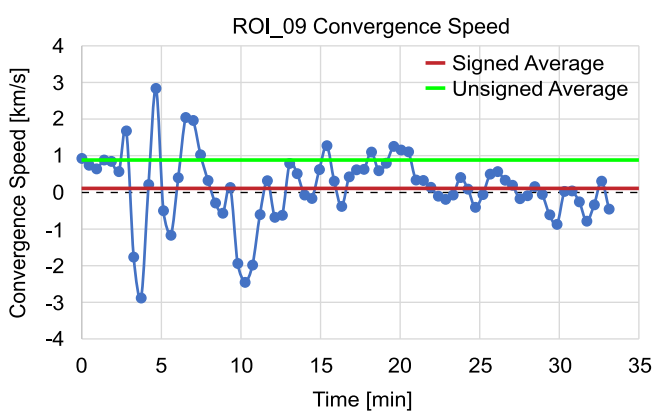

Figure 5. Convergence speed, v_{conv}, over the cancellation duration as calculated with the COG method for ROI_09. As the canceling features occasionally drift apart, v_{conv} becomes negative. The average v_{conv} for that event, 0.1 km s^{-1}, is represented by the red line. The proper motion speeds are calculated by $vv_{proper} = |v_{conv}|$, and the mean value is shown by the green line, which is 0.7 km s^{-1}. ROI_09 is shown here since it exhibits strong polarity drift.

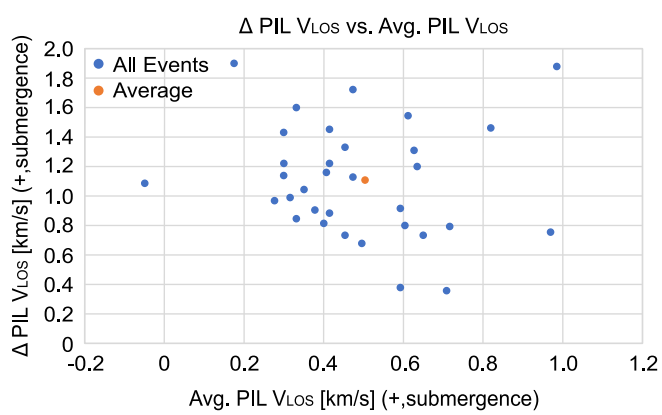

Figure 6. Scatter plot of ΔV_{LOS} vs. $V_{LOS,avg}$ for all events. Recall that ΔV_{LOS} is the difference between the extreme values of V_{LOS} over the lifetime of the event.

apparent with a more sensitive data set. We also analyzed the correlation between V_{LOS} and R for the 15, 10, and 5 strongest flux patches but found no correlation. It is possible that some

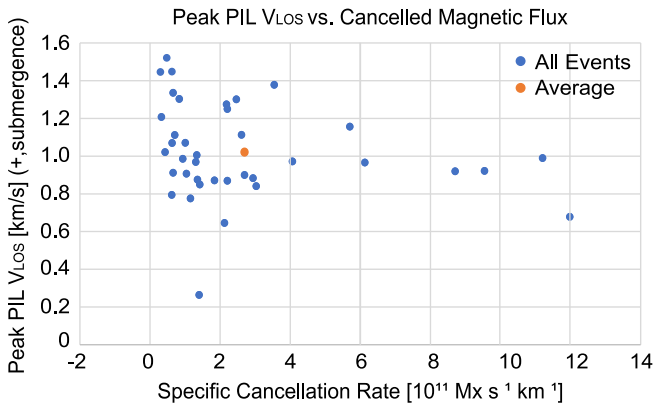

Figure 7. Scatter plot of peak Doppler velocity, $V_{\mathrm{LOS,peak}}$ vs. total canceled flux, $\Delta\Phi_B$ for all events.

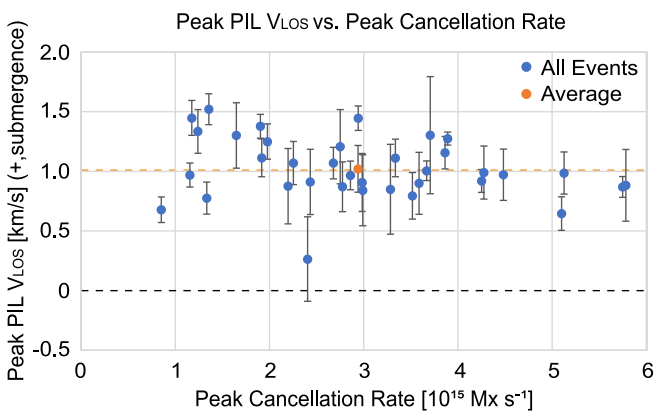

Figure 8. Scatter plot of peak Doppler velocity, $V_{\mathrm{LOS,peak}}$ vs. peak flux cancellation rate, R_{peak} for all events. Recall that positive values of R_{peak} indicate flux cancellation while negative values indicate flux accumulation.

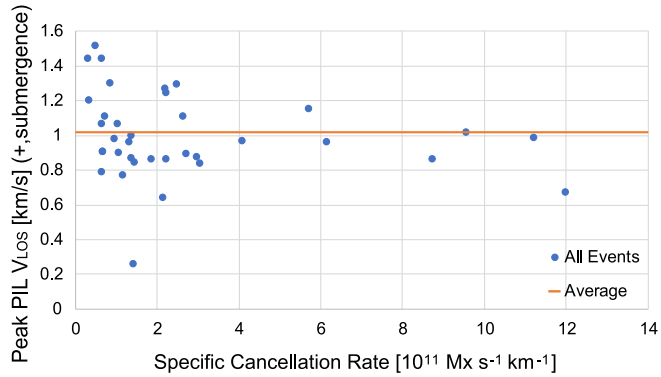

Figure 9. Scatter plot of peak Doppler velocity, $V_{\mathrm{LOS,peak}}$ vs. specific cancellation rate, r for all events. Recall that r measures cancellation per unit length of the PIL.

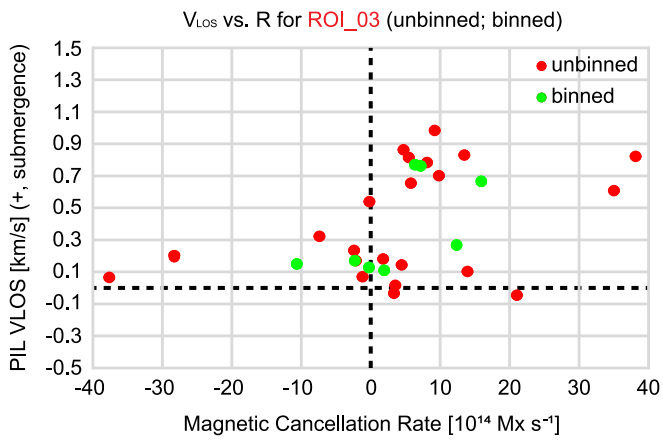

Figure 10. Scatter plot of Doppler velocity, V_{LOS} vs. flux cancellation rate, R for ROI_03. Unbinned and binned values are indicated.

undiscovered mechanism is creating a positive time separation between submergences and magnetic cancellation such that when the features dip below the instrument threshold even more of the downflows are lost due to background noise.

We calculated the error by taking the standard deviation divided by the square root of the number of frames in the sequence relevant to the cancellation event. Ultimately, the standard error represents the standard deviation of the mean within the data set.

Finally, we find that the specific cancellation rate, r, was correlated with R_{avg} ($R^2 = 0.707$). This indicates that the primary transport mechanism of magnetic flux out of the bipole is through the PIL.

5. Discussion and Conclusion

In this study, we used spectropolarimetric measurements from the SST to investigate the physical properties of magnetic cancellations in the QS photosphere. Examining an LOS magnetogram we visually identified 38 cancellations, and using the YAFTA program suite (Welsch et al. 2004), we tracked the magnetic elements involved in the cancellation and extracted their time-dependent physical parameters. We found that cancellations and downflows occur simultaneously, with an average relative speed of $\Delta V_{\mathrm{LOS}} = 1.1$ km s^{-1}. We found no increase in the linear polarization signal in our data, corresponding to the horizontal component of magnetic field B_t probably because it was below the noise level of the observations. This means that we cannot comment on whether the flux retracts below the photosphere and forms structures that could lead to reconnection. Our findings are consistent with the study in Kubo et al. (2010), which also did not find horizontal magnetic fields. A snapshot of the data is included in the Appendix. We expect that with more sensitive data these magnetic cancellations would be observed with enhanced B_t signals, providing stronger evidence of possible magnetic reconnection.

While establishing the link between downflows and cancellations is an important discovery in this study, we also calculated other statistical parameters that characterize these events: $\Phi_{B,i}$, $\Delta\Phi_B$, R_{avg}, R_{peak}, r, T, and v_{conv} (see Table 1).

Aside from v_{conv}, we estimated the proper motion of the magnetic elements by using the unsigned average of their speeds, $v_{\mathrm{proper}} = |v_{\mathrm{conv}}|$. While this is not the same method used by others, such as Kaithakkal & Solanki (2019), we found v_{proper} to be on average 1 km s^{-1}. This was significantly higher than the average speed of $v_{\mathrm{conv}} = 0.6 \pm 0.06$. Because the v_{conv} for individual events was highly variable (see Figure 5) and our new value of v_{proper} agreed with the rms velocity for magnetic IN elements (Nisenson et al. 2003), we assume that magnetic cancellations are driven by granular motions that force the magnetic elements into intergranular lanes where they cancel. In future studies, we would like to analyze the contribution of supergranular flows to the movement of the magnetic elements. Our exact value of v_{proper} is likely an underestimate since it is still a relative measurement.

Although our study identified many cancellations, their lifetimes were noise limited. In Section 5, we theorized that because of the instrument noise level some weak fields may not have been detected and tracked by the YAFTA program. This is evident by only around 45% of initial flux being canceled in an average magnetic bipole. Given the YAFTA parameters outlined in Section 2, we were unable to track polarities below the noise floor of the data set (Lamb et al. 2008). Because many of the events ended below the noise floor, this limited our analysis of the direct correlation between magnetic flux cancellation and plasma downflows.

Limiting our study to same-sized opposite-polarity elements and avoiding elements where same-signed flux recombined prevented us from detecting more events and thus led to an underestimation of magnetic flux evolution. In Figure 2 of Gošić et al. (2016) the authors present a methodology to track differently sized features. We may employ a similar method in future studies of IN magnetic elements.

Although we determined the optimal threshold to detect features in YAFTA, a more in-depth understanding of QS magnetism would be achieved by observations with larger-aperture telescopes, and more advanced tracking algorithms. In the YAFTA program we empirically determined both a minimum size and magnetic threshold that determined whether features were tracked. We did this by simply observing the point at which noise patterns were no longer detected as features by YAFTA, then used that threshold in the analysis of all the ROIs. As stated before, we excluded pixels below 40 G and magnetic elements under 4 pixels in size from our analysis. It is possible that algorithmically determining the exact thresholds for each ROI would yield better detection of the events near the end of their lifetimes.

Magnetic reconnection also may occur with U-loop emergences, which cause brightenings in the local chromosphere (Gošić et al. 2018; Kontogiannis et al. 2020, and others). In order to investigate the effects of small-scale reconnection events on the higher layers of the atmosphere, we plan to combine observations in photospheric (as those employed in this study) and chromospheric lines. In particular, we plan to acquire spectropolarimetric observations in Ca II 854.2 nm to investigate the evolution of the chromospheric magnetic field and broadband images in Ca II UV lines (e.g., the Ca II-H filter at the SST) to estimate the amount of energy released in the chromosphere during reconnection.

The statistical parameters found in our study are important for implicating magnetic cancellations in future studies of the QS and complement existing literature. Lastly, it would be interesting to reexamine QS magnetic fields using higher-aperture telescopes. Higher-aperture telescopes naturally have higher spatial resolution, which is required to resolve the PIL; better spectropolarimetric sensitivity is necessary to track features for longer times, and will increase the detectability of features and therefore increase the quality of the derived statistics. Spectropolarimetric measurements from existing and upcoming installments such as the Big Bear Solar Observatory, the European Solar Telescope (EST), and the Daniel K. Inouye Solar Telescope (DKIST; Rast et al. 2021), respectively, will allow for a more detailed study of the evolution of the magnetic field components.

This work was supported by NSF through award No. 1659878 for the Boulder Solar Alliance REU in 2019. F.Z. acknowledges support from the European Union's Horizon 2020 research and innovation program under the grant agreement Nos. 739500 (PRE-EST project) and 824135 (SOLARNET project), by the Universita degli Studi di Catania (PIA.CE.RI. 2020-2022 Linea 2), by the Italian MIUR-PRIN grant 2017APKP7T on "Circumterrestrial Environment: Impact of Sun-Earth Interaction". The National Solar Observatory is operated by the Association of Universities for Research in Astronomy, Inc. (AURA) under a cooperative agreement with the National Science Foundation. The Swedish 1-m Solar Telescope is operated on the island of La Palma by the Institute for Solar Physics of Stockholm University in the Spanish Observatorio del Roque de los Muchachos of the Instituto de Astrofísica de Canarias. The Institute for Solar Physics is supported by a grant for research infrastructures of national importance from the Swedish Research Council (registration number 2017-00625). This research is supported by the Research Council of Norway, project number 250810, and through its Centers of Excellence scheme, project number 262622. M.D.K. acknowledges support from NASA ECIP NNH18ZDA001N and NSF CAREER SPVKK1RC2MZ3. We made much use of NASA's Astrophysics Data System bibliographic services. We wish to thank the US Taxpayers for their generous support for this project.

Appendix

In this appendix we describe the evolution of four more cancellations in detail—ROI_07, ROI_08, ROI_11, and ROI_23. These events are shown in context with the data sets in Figures 1 and 2.

A.1. Analysis of ROI_07

ROI_07 involves a larger negative polarity and smaller positive polarity canceling in an intergranular lane, as illustrated in Figure 11. $\Phi_{B,i}^{-}$ was 4.1×10^{17} Mx and $\Phi_{B,i}^{+}$ was 1.1×10^{17} Mx. As shown in Figure 12, after approximately 13 minutes the bipole lost 49.7% of its initial magnetic flux, or 2.6×10^{17} Mx. During the cancellation the positive and negative polarities lose 0.7×10^{17} and 1.9×10^{17} Mx, respectively. The average cancellation rate was 3.7×10^{14} Mx s^{-1}. Within about 2 minutes of canceling there was a 0.6 km s^{-1} increase in submergence speed, then a gradual oscillation and decrease to around 0 km s^{-1}.

A.2. Analysis of ROI_08

In ROI_08 we see cancellation occurring by examining the top row of Figure 13. Examining continuum imagery, we see the cancellation occurred in an intergranular lane. Positive polarity labeled 87 and negative polarity labeled 92, seen in Figure 13 begin canceling at 08:21:27 UTC and the event lasts until 08:41:03 UTC. $\Phi_{B,i}^{-}$ was 2.1×10^{17} Mx and $\Phi_{B,i}^{+}$ was 4.02×10^{17} Mx and during the cancellation the positive and negative polarities lose 1.2×10^{17} and 1.8×10^{17} Mx, respectively. About 50% of the initial bipole magnetic flux was lost during the cancellation event. The average cancellation rate through the event was 2.5×10^{14} Mx s^{-1}. Visual inspection of the magnetograms in Figure 13, reveals that both the positive and negative polarities lose apparent size as they cancel, with the negative polarity falling below the instrument noise level in panel (a7). Figure 14 shows that within roughly

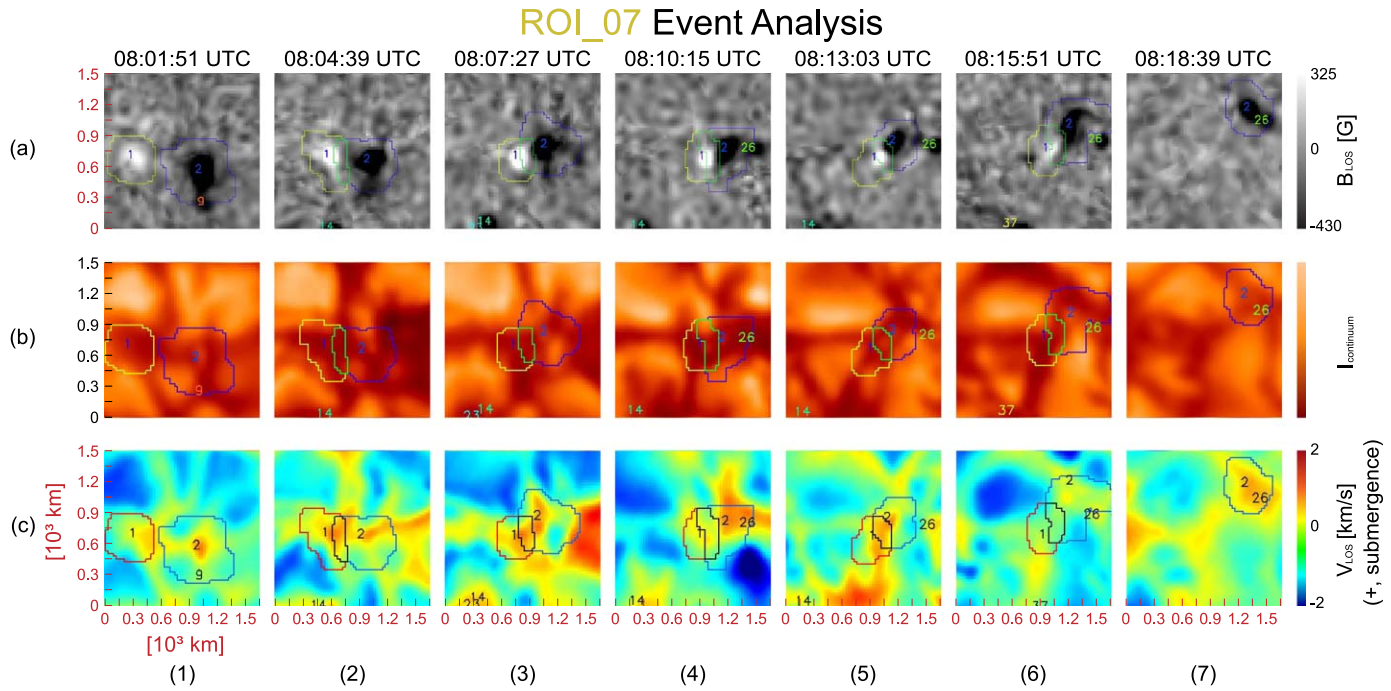

Figure 11. Evolution of $B_{\rm LOS}$ (top series), 630.1 nm intensity (middle series), and $V_{\rm LOS}$ (bottom series). ROI_07 in the time series begins with panel 1 (time immediately before PIL is defined) and progresses to panel (7) (time immediately after PIL is no longer defined).

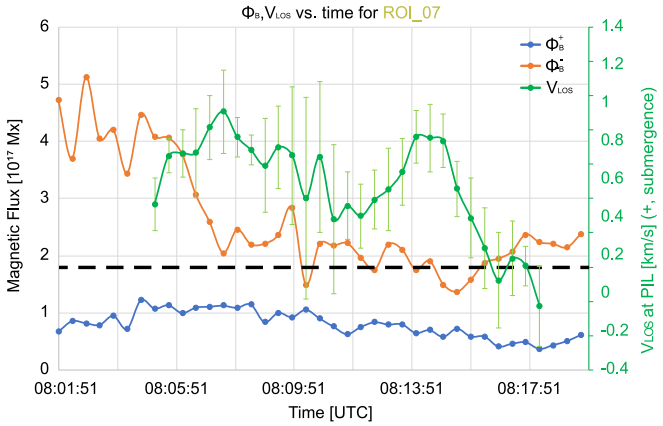

Figure 12. Evolution of LOS magnetic flux and PIL mean Doppler velocity, Φ_B and $V_{\rm LOS}$, in ROI_07. Refer to the caption of Figure 4 for an explanation of the legend and other graphical details.

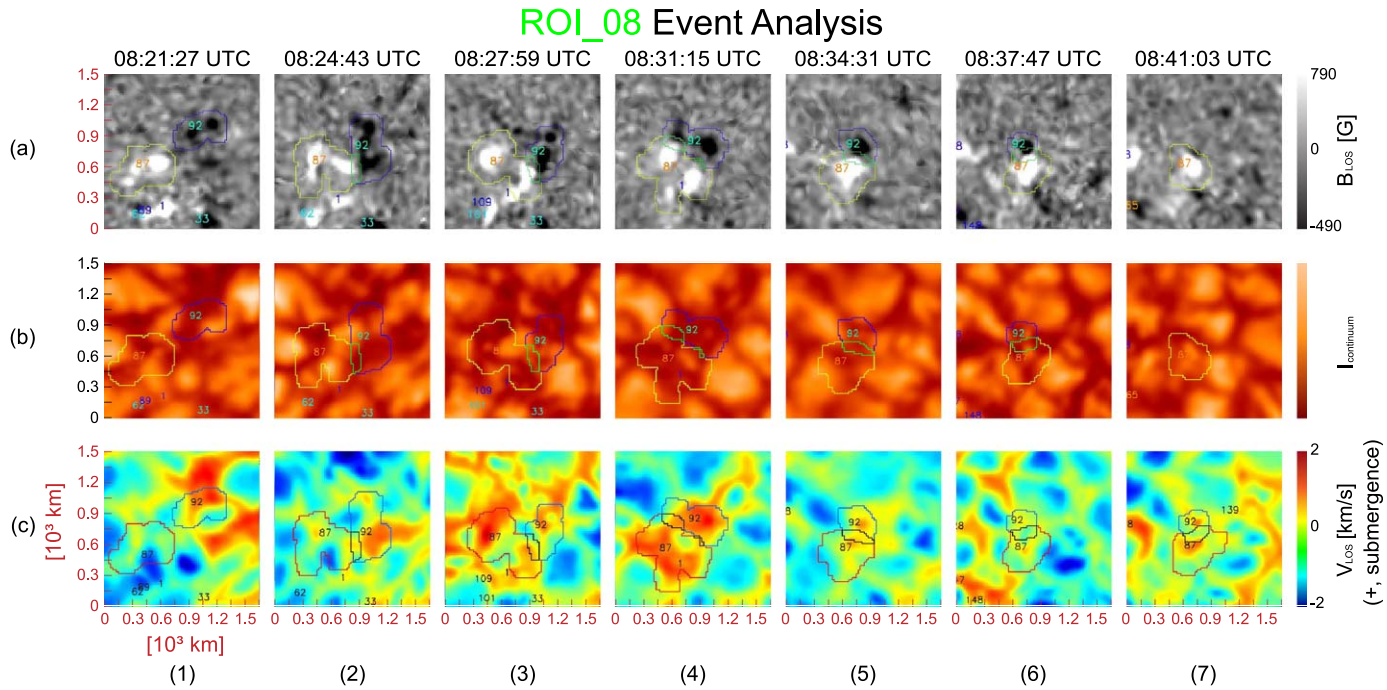

Figure 13. Evolution of B_{LOS} (top series), 630.1 nm intensity (middle series), and V_{LOS} (bottom series). ROI_08 in the time series begins with panel (1) (time immediately before the PIL is defined) and progresses to panel (7) (time immediately after PIL is no longer defined).

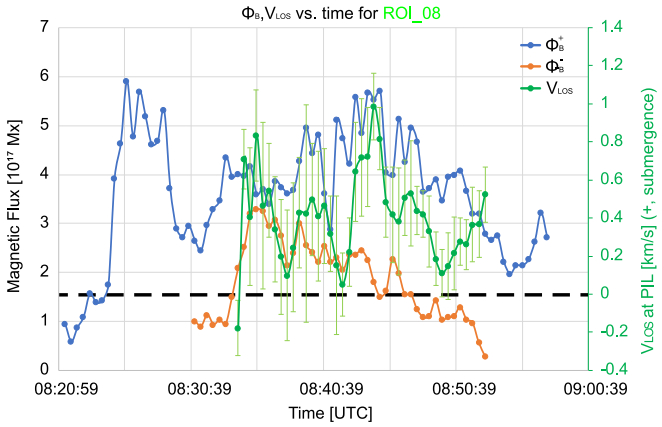

Figure 14. Evolution of LOS magnetic flux and PIL mean Doppler velocity, Φ_{B} and V_{LOS}, in ROI_08. Refer to the caption of Figure 4 for an explanation of the legend and other graphical details.

2 minutes after first canceling the Doppler velocity at the PIL jumps from -0.2 to 0.8 km s^{-1}. Following that initial increase, the Doppler velocity is relatively variable but still higher than the initial -0.2 km s^{-1} detected.

A.3. Analysis of ROI_11

ROI_11 involved a small positive polarity (0.9×10^{17} Mx) and a large negative polarity (7.4×10^{17} Mx) that canceled over the course of around 18 minutes. The cancellation began in a downflow of 0.3 km s^{-1} and the submergence speed peaked at around 0.8 km s^{-1}, the same time as the cancellation rate peaked ($R_{\mathrm{peak}} = 27 \times 10^{14}$ Mx). The positive polarity gained a small amount of flux during the event, around 0.1×10^{17} Mx while the negative polarity's flux decreased by almost 30% or 2.4×10^{17} Mx. These values can be inferred from the inspection of Figure 15. Analyzing the B_{LOS}, $I_{\mathrm{continuum}}$, and V_{LOS} images in Figure 16, we can see in continuum imagery that the cancellation begins in an intergranular lane (dark patch). This is supported by the starting V_{LOS} of 0.3 km s^{-1}. In B_{LOS} we can see the positive polarity patch labeled 8 and negative polarity patch labeled 98 interacting throughout the time series and eventually the positive polarity moves out of the ROI in the last time step. In panel (4c) we see the greatest intensification of the V_{LOS}. In panel (3a) we see the positive polarity briefly dip below the noise threshold then it is relabeled in panel (4a).

A.4. Analysis of ROI_23

ROI_23 involves a large positive polarity (1.0×10^{17} Mx) and a small negative polarity (0.5×10^{17} Mx). The cancellation lasted 28 minutes and reached a maximum Doppler velocity of $V_{\mathrm{LOS}} = 1.1$ km s^{-1}. This event is different from most in that it begins in an upflow of roughly 0.3 km s^{-1} and ends in a

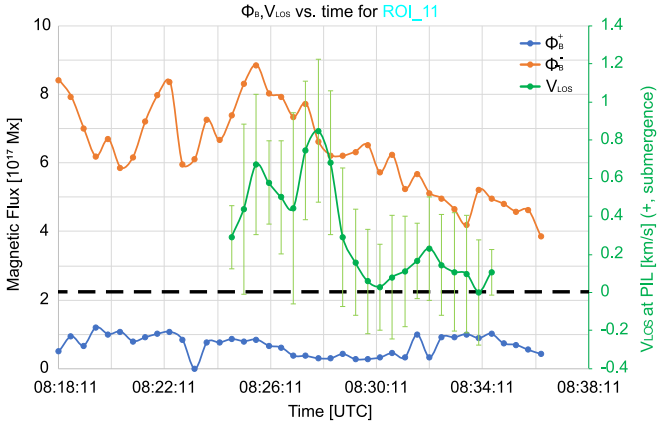

Figure 15. Evolution of LOS magnetic flux and PIL mean Doppler velocity, Φ_B and $V_{\rm LOS}$, in ROI_11. Refer to the caption of Figure 4 for an explanation of the legend and other graphical details.

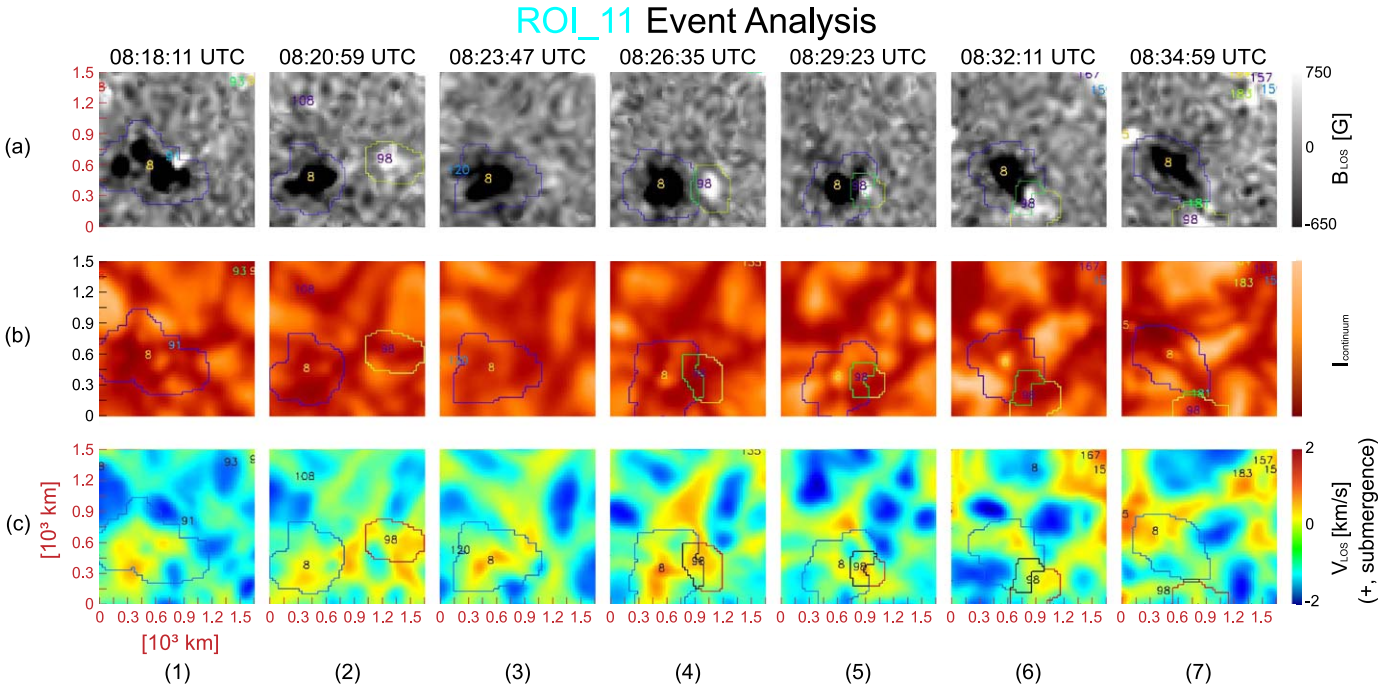

Figure 16. Evolution of $B_{\rm LOS}$ (top series), 630.1 nm intensity (middle series), and $V_{\rm LOS}$ (bottom series). ROI_11 in the time series begins with panel (1) (time immediately before the PIL is defined) and progresses to panel (7) (time immediately after the PIL is no longer defined).

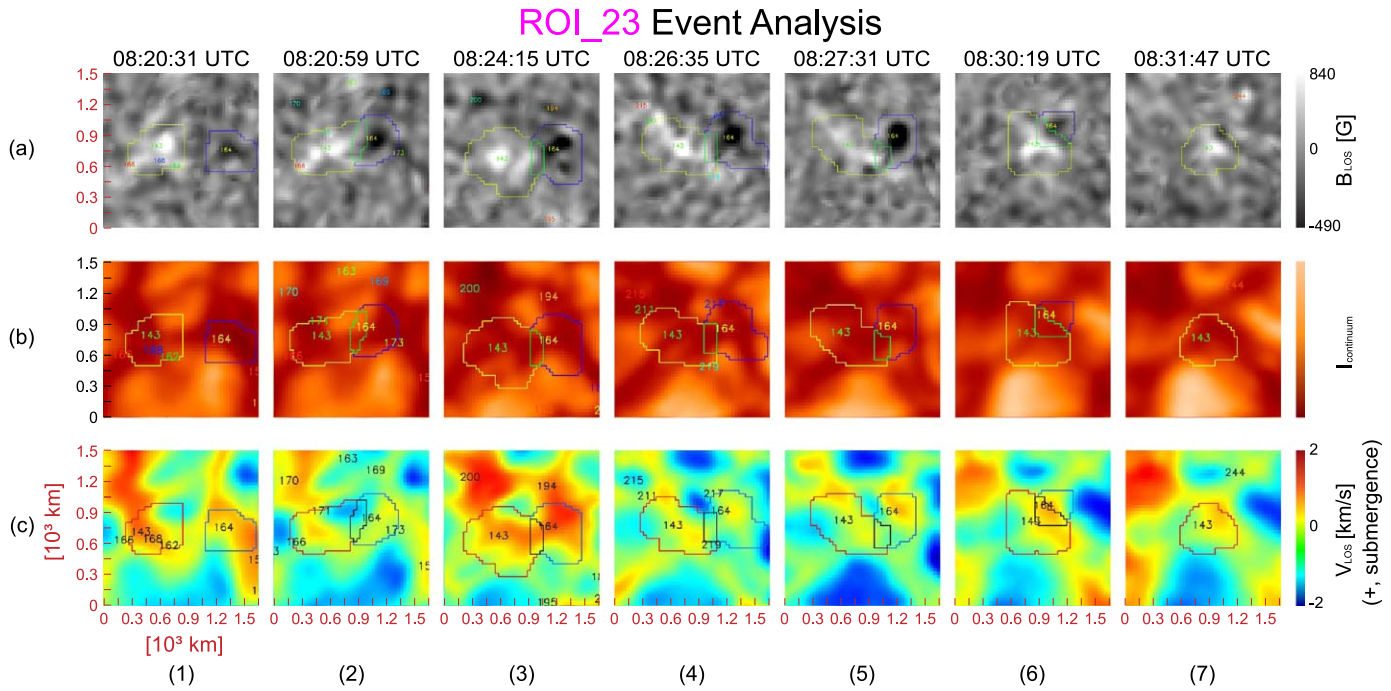

Figure 17. Evolution of $B_{\rm LOS}$ (top series), 630.1 nm line core (middle series), and $V_{\rm LOS}$ (bottom series). ROI_23 in the time series begins with panel (1) (time immediately before the PIL is defined) and progresses to panel (7) (time immediately after the PIL is no longer defined).

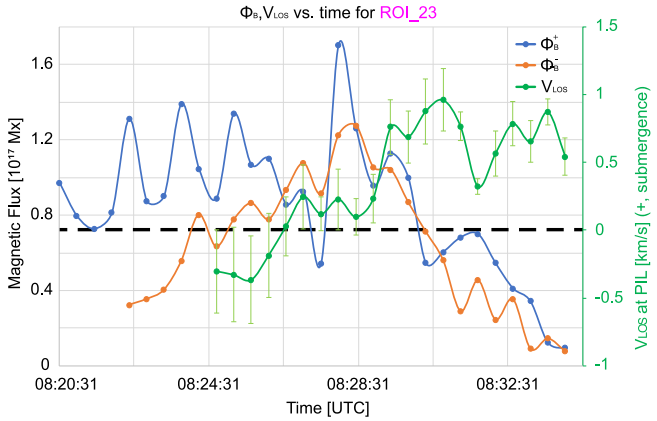

Figure 18. Evolution of LOS magnetic flux and PIL mean Doppler velocity, Φ_B and $V_{\rm LOS}$, in ROI_23. Refer to the caption of Figure 4 for an explanation of the legend and other graphical details.

downflow of roughly 1.1 km^{-1} meaning that the $\Delta V_{\rm LOS}$ of this event is large, $\approx$1.4 km s^{-1}. Both Figure 17 and the plot in Figure 18 show that this is a very clear case of cancellation ending in a downflow region in an intergranular lane.

ORCID iDs

Vincent E. Ledvina https://orcid.org/0000-0003-0127-5105
Maria D. Kazachenko https://orcid.org/0000-0001-8975-7605
Serena Criscuoli https://orcid.org/0000-0002-4525-9038
Dennis Tilipman https://orcid.org/0000-0001-9361-6629
Ilaria Ermolli https://orcid.org/0000-0003-2596-9523
Mariachiara Falco https://orcid.org/0000-0002-0018-6488
Salvatore Guglielmino https://orcid.org/0000-0002-1837-2262
Shahin Jafarzadeh https://orcid.org/0000-0002-7711-5397
Luc Rouppe van der Voort https://orcid.org/0000-0003-2088-028X
Francesca Zuccarello https://orcid.org/0000-0003-1853-2550

References

Bellot Rubio, L., & Orozco Suárez, D. 2019, LRSP, 16, 1
Bellot Rubio, L. R., & Orozco Suárez, D. 2012, ApJ, 757, 19
Chae, J., Moon, Y.-J., & Pevtsov, A. A. 2004, ApJL, 602, L65
Chae, J., Moon, Y.-J., Wang, H., & Yun, H. S. 2002, SoPh, 207, 73
Chintzoglou, G., Zhang, J., Cheung, M. C. M., & Kazachenko, M. 2019, ApJ, 871, 67
Cristaldi, A., & Ermolli, I. 2017, ApJ, 841, 115
Criscuoli, S., & Foukal, P. 2017, ApJ, 835, 99
Danilovic, S., Beeck, B., Pietarila, A., et al. 2010, ApJL, 723, L149
de la Cruz Rodríguez, J., Löfdahl, M. G., Sütterlin, P., Hillberg, T., & Rouppe van der Voort, L. 2015, A&A, 573, A40
De Pontieu, B., Title, A. M., Lemen, J. R., et al. 2014, SoPh, 289, 2733
de Wijn, A. G., Lites, B. W., Berger, T. E., et al. 2008, ApJ, 684, 1469
DeForest, C. E., Hagenaar, H. J., Lamb, D. A., Parnell, C. E., & Welsch, B. T. 2007, ApJ, 666, 576
del Toro Iniesta, J. C. 2007, Introduction to Spectropolarimetry (Cambridge: Cambridge Univ. Press)
del Toro Iniesta, J. C., & Ruiz Cobo, B. 2016, LRSP, 13, 4
Denker, C., & Tritschler, A. 2009, in IAU Symp. 259 (Cambridge: Cambridge Univ. Press), 223
Dravins, D., Lindegren, L., & Nordlund, A. 1981, A&A, 96, 345
Faurobert, M., Balasubramanian, R., & Ricort, G. 2016, A&A, 595, A71
Gošić, M. 2015, PhD thesis, Universidad de Granada
Gošić, M., Bellot Rubio, L. R., del Toro Iniesta, J. C., Orozco Suárez, D., & Katsukawa, Y. 2016, ApJ, 820, 35
Gošić, M., Bellot Rubio, L. R., Orozco Suárez, D., Katsukawa, Y., & del Toro Iniesta, J. C. 2014, ApJ, 797, 49
Gosic, M., de la Cruz Rodriguez, J., De Pontieu, B., et al. 2017, AGUFM, 2017, #SH41C-02
Gošić, M., de la Cruz Rodríguez, J., De Pontieu, B., et al. 2018, ApJ, 857, 48
Gosic, M., De Pontieu, B., & Bellot Rubio, L. R. 2021, ApJ, 911, 41
Gosic, M., Katsukawa, Y., Bellot Rubio, L., & Orozco Suarez, D. 2012, in 39th COSPAR Scientific Assembly (Paris: ESA), 657
Guglielmino, S. L., Martínez Pillet, V., Bonet, J. A., et al. 2012, ApJ, 745, 160

Harvey, J. 1971, PASP, 83, 539
Harvey, K. L., Jones, H. P., Schrijver, C. J., & Penn, M. J. 1999, SoPh, 190, 35
Iida, Y., Hagenaar, H. J., & Yokoyama, T. 2012, ApJ, 752, 149
Kaithakkal, A. J., & Solanki, S. K. 2019, A&A, 622, A200
Keys, P. H., Mathioudakis, M., Jess, D. B., et al. 2011, ApJL, 740, L40
Kontogiannis, I., Tsiropoula, G., Tziotziou, K., et al. 2020, A&A, 633, A67
Kubo, M., Low, B. C., & Lites, B. W. 2010, ApJ, 712, 1321
Lamb, D. A., DeForest, C. E., Hagenaar, H. J., Parnell, C. E., & Welsch, B. T. 2008, ApJ, 674, 520
Lamb, D. A., Howard, T. A., DeForest, C. E., Parnell, C. E., & Welsch, B. T. 2013, ApJ, 774, 127
Litvinenko, Y. E., Chae, J., & Park, S.-Y. 2007, ApJ, 662, 1302
Livi, S. H. B., Wang, J., & Martin, S. F. 1985, AuJPh, 38, 855
Livingston, W. C., & Harvey, J. 1975, BAAS, 7, 346
Martin, S. F., Livi, S. H. B., & Wang, J. 1985, AuJPh, 38, 929
Martínez González, M. J., & Bellot Rubio, L. R. 2009, ApJ, 700, 1391
Nisenson, P., van Ballegooijen, A. A., de Wijn, A. G., & Sütterlin, P. 2003, ApJ, 587, 458
Oba, T., Iida, Y., & Shimizu, T. 2017, ApJ, 836, 40
Panesar, N. K., Sterling, A. C., Moore, R. L., & Chakrapani, P. 2016, ApJL, 832, L7
Park, S., Chae, J., & Litvinenko, Y. E. 2009, ApJL, 704, L71
Rast, M. P., Bello González, N., Bellot Rubio, L., et al. 2021, SoPh, 296, 70
Rees, D. E., & Semel, M. D. 1979, A&A, 74, 1
Rempel, M. 2014, ApJ, 789, 132
Rempel, M. 2020, ApJ, 894, 140
Sánchez Almeida, J. 2004, in ASP Conf. Ser., 325, The Magnetism of the Very Quiet Sun, ed. T. Sakurai & T. Sekii (San Francisco, CA: ASP), 115
Scharmer, G. B., Bjelksjo, K., Korhonen, T. K., Lindberg, B., & Petterson, B. 2003a, Proc. SPIE, 4853, 341
Scharmer, G. B., Dettori, P. M., Löfdahl, M. G., & Shand, M. 2003b, Proc. SPIE, 4853, 370
Scharmer, G. B., Narayan, G., Hillberg, T., et al. 2008, ApJL, 689, L69
Schmieder, B., Pariat, E., Aulanier, G., et al. 2002, in ESA Special Publication, Vol. 2, Solar Variability: From Core to Outer Frontiers, ed. A. Wilson (Prague: ESA), 911
Schrijver, C. J., Title, A. M., van Ballegooijen, A. A., Hagenaar, H. J., & Shine, R. A. 1997, ApJ, 487, 424
Stangalini, M., Giannattasio, F., Erdélyi, R., et al. 2017, ApJ, 840, 19
Stangalini, M., Giannattasio, F., & Jafarzadeh, S. 2015, A&A, 577, A17
Thornton, L. M., & Parnell, C. E. 2011, SoPh, 269, 13
Uitenbroek, H. 2003, ApJ, 592, 1225
van Noort, M., Rouppe van der Voort, L., & Löfdahl, M. G. 2005, SoPh, 228, 191
Viavattene, G., Murabito, M., Guglielmino, S. L., et al. 2021, Entrp, 23, 413
Wang, J., Shi, Z., & Martin, S. F. 1996, A&A, 316, 201
Welsch, B. T., Fisher, G. H., Abbett, W. P., & Regnier, S. 2004, ApJ, 610, 1148
Yang, S., Zhang, J., & Borrero, J. M. 2009, ApJ, 703, 1012
Yardley, S. L., Green, L. M., Williams, D. R., et al. 2016, ApJ, 827, 151
Zhang, J., Wang, J., Deng, Y., & Wu, D. 2001, ApJL, 548, L99
Zirin, H. 1985, AuJPh, 38, 961
Zuccarello, F., Battiato, V., Contarino, L., Romano, P., & Spadaro, D. 2007, A&A, 468, 299